

## Multimode Rayleigh-Taylor Experiments on Nova

B. A. Remington, S. V. Weber, M. M. Marinak, S. W. Haan, J. D. Kilkenny, R. Wallace, and G. Dimonte

Lawrence Livermore National Laboratory, Livermore, California 94551

(Received 2 February 1994)

Multimode Rayleigh-Taylor experiments have been conducted with planar CH(Br) foils accelerated by x-ray ablation. The perturbations consisted of the superposition of either two or eight sinusoids. In the linear regime the modes grow independently, but become coupled in the nonlinear regime, leading to the appearance of  $k_i \pm k_j$  "beat" modes. This results in a redistribution of the perturbation into a broader Fourier spectrum causing a change of shape: bubbles become broader and spikes narrower. The overall size of the perturbation is not significantly altered.

PACS numbers: 52.35.Py, 47.40.-x, 52.65.+z, 52.70.La

The Rayleigh-Taylor (RT) instability has been the focus of hydrodynamics research in inertial confinement fusion (ICF) for some time [1–16]. In ICF, the drive (laser light, x rays, or ion beams) heats the outer layer of the capsule wall, causing it to ionize and rapidly expand. In reaction, strong shocks are launched through the cold dense material ahead of the ablation front (the "pusher"), after which the pusher accelerates radially inwards, compressing ("implosion") the D,T nuclear fuel contained inside. During the shock transit phase, perturbations at the surface or at any interface will grow due to the Richtmyer-Meshkov instability [17,18], the impulsive analog of the RT instability. During the acceleration phase, a low density ablated plasma is accelerating the high density pusher, and the ablation front is RT unstable. Outer surface imperfections will grow further and eventually perturb the inner surface, which in turn becomes RT unstable during the deceleration phase of the implosion. Pusher material can mix into the fuel degrading performance [1–3,19].

The linear regime of the RT instability is defined by  $\eta/\lambda \ll 1$ , where  $\eta$  and  $\lambda$  represent the perturbation amplitude and wavelength. In the linear regime, single-mode perturbations grow exponentially,  $\eta = \eta_0 e^{\gamma t}$ . The growth rate  $\gamma$  is given by  $\gamma \approx (\alpha kg)^{1/2} - \beta k v_a$ , where  $\alpha = (1 + kL)^{-1}$  and  $v_a = \dot{m}/\rho_{\max}$ . Here  $k = 2\pi/\lambda$  is the perturbation wave number,  $L = \rho/\nabla\rho$  is the density gradient scale length,  $g$  is the acceleration,  $\dot{m}$  is the mass ablation rate per unit area,  $\rho_{\max}$  is the foil maximum density, and  $\beta \approx 2-3$  is a multiplier on the ablative term [4,5]. After sufficient growth,  $\eta/\lambda \geq 0.1$ , the perturbation enters the nonlinear regime, and its shape changes from sinusoidal to "bubble and spike" [3]. The growth slows and in the asymptotic limit the bubble amplitude can be written as  $\eta = \int v_b dt$ , where  $v_b \approx 0.3\sqrt{g\lambda}$  represents the terminal bubble velocity [20]. Capsule surface finishes are not single mode, however, but multimode in nature. When more than one mode is present, the modes grow independently in the linear regime but become coupled in the nonlinear regime, leading to the appearance of "beat" modes,  $k_i \pm k_j$ . This causes a redistribution of the perturbation to longer and shorter wavelengths,

changing the shape of the perturbation and affecting the saturation of individual modes [13–16]. It is this multimode growth and saturation that ultimately affects ICF capsule performance. We present here the first experimental study of mode coupling and nonlinear multimode saturation in ablatively accelerated foils.

The experimental setup is illustrated in Fig. 1. Sinusoidal surface perturbations are molded onto one side of a planar 750  $\mu\text{m}$  diameter,  $\sim 50 \mu\text{m}$  thick,  $\rho = 1.26 \text{ g/cm}^3$  CH(Br) foil ( $\text{CH}_{1-x}\text{Br}_x$  with  $x = 0.054$ ). The foil is mounted across a hole in the wall of a 3000  $\mu\text{m}$  long, 1600  $\mu\text{m}$  diameter gold cylindrical hohlraum with the perturbations facing inwards. The foil is diagnosed by back illumination with a  $\sim 700 \mu\text{m}$  diameter spot of x rays created by irradiating a rhodium disk with a single Nova beam [21] of wavelength, energy, and temporal shape of 0.53  $\mu\text{m}$ , 2.5 kJ, and 5 ns square, respectively. The Rh L-band x rays to which the detector is sensitive have a mean free path of  $\sim 20 \mu\text{m}$  in the CH(Br) foils. The transverse modulations in foil areal density ( $\int \rho dz$ ) cause modulations in the optical depth of the foil. Hence,

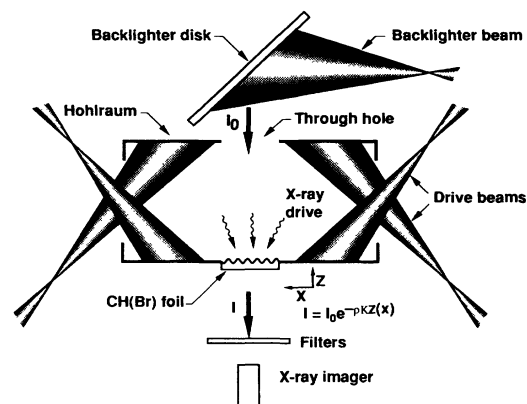


FIG. 1. The experimental configuration consists of a Au cylindrical hohlraum with a modulated CH(Br) foil mounted on the wall. The laser beams convert to x rays in the hohlraum which ablatively accelerate the foil. An additional laser beam generates backlighter x rays used for in flight diagnosis of the foil.

the transmitted backlighter x-ray flux, given by

$$I(x, t) = I_0(t) e^{-\int K \rho dz}, \quad (1)$$

bears the imprint of the modulated foil. The  $K$  corresponds to foil opacity, and is calculated independently using the supertransition array model [22]. Hence, growth of modulations in areal density can be deduced from transmission measurements of  $I(x, t)$ . The time-resolved image,  $I(x, t)$ , is recorded onto film using a  $22\times$  magnification streaked Wölter x-ray microscope [23]. Only modulations of  $I(x, t)$  in the transverse ( $\hat{x}$ ) spatial direction are of interest; time-dependent variations of the overall backlighter brightness divide out in the analysis. The instrument spatial resolution is critical to proper interpretation of the data, and is expressed as the modulation transfer function. This represents the ratio of observed to actual contrast, and for these experiments is given by  $M(k) = 1/[1 + (k\sigma)^2]$ , with  $\sigma = 6.3 \mu\text{m}$ .

The low adiabat x-ray drive used here and in our previous work [10–12] is shown in Fig. 2. It was generated by focusing eight  $0.35 \mu\text{m}$ , 2.2 kJ, 3.3 ns temporally shaped Nova beams into the Au hohlraum, where they convert to mostly thermal x rays. The summed power of the eight lasers on a typical shot is given by the solid curve. The x-ray drive has been characterized by three independent experimental techniques: (1) a direct measurement of the x-ray drive spectrum emerging from the hohlraum using a filtered photodiode array [24], (2) shock breakout trajectory through an Al wedge mounted on the hohlraum and viewed with a streaked UV imager [21], and (3) accelerated foil trajectory using streaked side-on radiography [10,11]. The dotted curve shows an experimental radiation temperature  $T_r$  deduced from method (1), and the dot-dashed curve gives the “best fit”  $T_r$  to all three techniques, which represents the drive model used in the analysis presented

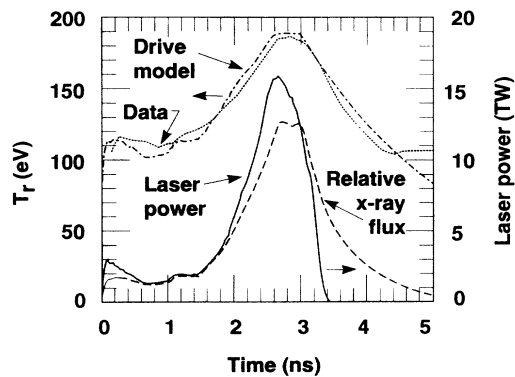


FIG. 2. The total power versus time of the  $\lambda = 1/3 \mu\text{m}$  drive lasers is shown as the solid curve and the scale on the right, and a measurement of the corresponding radiation temperature is given by the dotted curve and the scale on the left. The adopted drive temperature is the “best fit” to three independent measurements and is shown by the dot-dashed curve. The resulting relative x-ray flux is given by the dashed curve.

here. The corresponding relative x-ray flux is given by the dashed curve. The foil trajectories and hence the gross hydrodynamics are reproduced very well with this drive [11].

The multimode initial perturbations investigated are of the form  $\eta(x) = \sum \eta_n \cos(k_n x)$  and are shown in Fig. 3(a). The upper side of each curve corresponds to the foil. At the top is a large amplitude two-mode perturbation given by  $\lambda_2 = 75 \mu\text{m}$ ,  $\lambda_3 = 50 \mu\text{m}$ , and  $\eta_2 = \eta_3 = 2 \mu\text{m}$ , where the modes are enumerated as harmonics of the longest repeating pattern (here,  $150 \mu\text{m}$ ). At the bottom of Fig. 3(a), we show a small amplitude eight-mode perturbation given by  $\lambda_n = (180 \mu\text{m})/n$ ,  $n = 1-8$ . The amplitudes  $\eta_n$ , given in the figure caption, are on average a factor of 10 smaller than those of the two-mode foil. The initial perturbations are characterized by three independent techniques—interferometry, contact profilometry, and x-ray radiography—and are accurate to 10% or better.

In Fig. 3(b) we show the expected shapes of the perturbations late in time based on simulations using the 2D radiation-hydrodynamics code LASNEX [25]. The solid curves correspond to the multimode simulations and the dashed curves represent the sum of the results where each

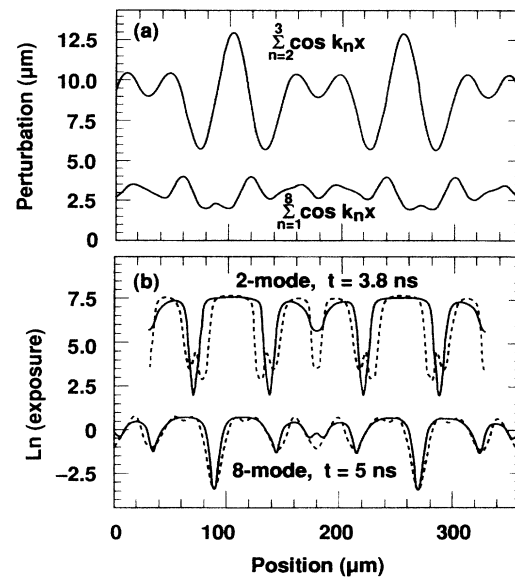


FIG. 3. In (a) the initial perturbation patterns investigated are shown. The upper curve corresponds to a  $\lambda_{2,3} = 75$  and  $50 \mu\text{m}$ ,  $\eta_{2,3} = 2 \mu\text{m}$  perturbation imposed on a  $54 \mu\text{m}$  thick CH(Br) foil. The lower curve corresponds to the sum of eight modes imposed on a  $50 \mu\text{m}$  thick CH(Br) foil with wavelengths  $\lambda_n = (180 \mu\text{m})/n$ ,  $n = 1-8$ , and amplitudes  $\eta_{1-8} = -0.2939, -0.2770, -0.3153, -0.3156, 0.2319, 0.1830, 0.1326,$  and  $-0.05867 \mu\text{m}$ . (b) The solid curves show  $\ln(\text{exposure})$  results from numerical simulations of the same perturbations after substantial Rayleigh-Taylor growth. The dashed curves show the same except in the absence of mode coupling. The effect of the instrument spatial resolution has not been included in these simulations.

individual mode was run alone. The perturbations evolve into broad bubbles penetrating into the foil, corresponding to regions of high  $\ln(\text{exposure})$ , and dense narrow spikes. The effect of mode coupling is readily apparent: the dominant bubbles become broader and the dominant spikes narrower. The overall size (e.g., rms) of the perturbation, however, is not significantly different due to mode coupling.

We next turn to the experimental results. Presentation of the data in Fourier space is the most illustrative. In Fig. 4 we show the Fourier spectrum of  $\ln(\text{exposure})$  from the accelerated two-mode foil at two times. At 2.0 ns, the total growth is small, about a factor of 2, and only the two preexisting modes,  $k_2$  and  $k_3$ , appear. Since the initial amplitudes are quite large, the perturbation quickly evolves into the nonlinear regime with the appearance at 3.3 ns of the second harmonic of  $k_2$ , namely,  $2k_2$ . We also observe very distinct  $k_3 - k_2$  and  $k_3 + k_2$  coupled modes corresponding to  $\lambda = 150$  and  $30 \mu\text{m}$ , respectively. Notably absent is the second harmonic of  $k_3$ , namely,  $2k_3$ . This is because  $3k_2$ , the third harmonic of  $k_2$ , has the same  $k$  but the opposite sign as  $2k_3$ , leading to a cancellation. The results from 2D LASNEX simulations are shown with the dashed histograms. The calculations slightly overpredict the observed growth, but the shapes of the Fourier spectra are in good qualitative agreement.

It is instructive to view these nonlinear effects within the context of second-order perturbation theory [15]. For a 2D multimode cosine perturbation at an interface of Atwood number  $A = (\rho_1 - \rho_2) / (\rho_1 + \rho_2) \approx 1$ , the spatial amplitude of mode  $k$  as a function of time can be written as

$$\eta_k(t) \approx \eta_k^L(t) + \frac{1}{2} k \left[ \sum_{k'} \eta_{k'}^L(t) \eta_{k+k'}^L(t) - \frac{1}{2} \sum_{k' < k} \eta_{k'}^L(t) \eta_{k-k'}^L(t) \right], \quad (2)$$

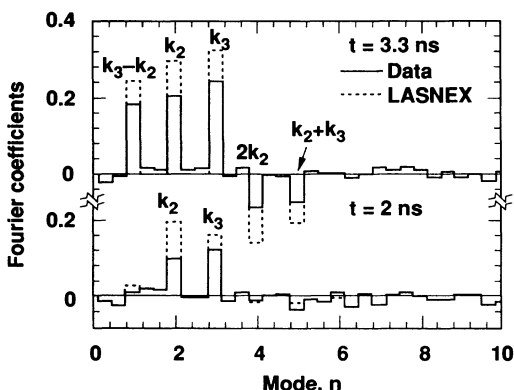


FIG. 4. The solid histograms represent the experimental Fourier spectra of  $\ln(\text{exposure})$  corresponding to the two-mode foil at 2.0 ns (bottom) and at 3.3 ns (top). The dashed histograms represent the numerical simulations with LASNEX, including the instrument spatial resolution.

where  $k, k' > 0$ , the superscript  $L$  denotes growth in the linear regime, and we have assumed that  $\gamma_k \propto \sqrt{k}$ . This model is implemented quantitatively below, but we consider here a qualitative description for the two modes  $k_2$  and  $k_3$ . For  $k = k_3 \pm k_2$ , it is straightforward to show that Eq. (2) reduces to

$$\eta_{k_3 \pm k_2}(t) \approx \mp \frac{1}{2} (k_3 \pm k_2) \eta_{k_2}^L(t) \eta_{k_3}^L(t), \quad (3)$$

where  $\eta_{k_n}^L$  represents the spatial amplitude of mode  $k_n$  had the growth been entirely in the linear regime. Notice that  $\eta_{k_3 - k_2}$  has the same sign as the product  $\eta_{k_2}^L \eta_{k_3}^L$ , whereas  $\eta_{k_3 + k_2}$  has the opposite sign, in agreement with the data and simulations shown in Fig. 4.

Consider next the small amplitude, eight-mode foil. In Fig. 5 we show the time evolution of the dominant modes,  $k_{1-4}$ . The data, represented by the open circles, correspond to the real component of the Fourier transform of  $\ln(\text{exposure})$ . Because of the cosine symmetry of the perturbation, the imaginary component should be identically zero, and is taken as an estimate of the error bars, typically  $\sim 20\%$ . The solid curves correspond to the eight-mode LASNEX simulation and the agreement with the data is quite good. The dashed curves represent simulations for each mode individually. (Similar single-mode simulations have been tested favorably against data on separate shots for perturbations of  $\lambda = 30, 50, 70$ , and  $100 \mu\text{m}$ .) The  $k_1$  mode is a particularly interesting case. The sign of its initial perturbation is negative [see the caption for Fig. 3(a)], and had it grown alone it would have maintained this sign, as shown by the dashed curve in Fig. 5. Late in time, however, the observed  $k_1$  mode is distinctly positive. This multimode effect can be qualitatively understood from Eq. (3). Both the  $k_3 - k_2$  and  $k_4 - k_3$  coupled terms are positive, tending to cause a phase reversal in the growth of the  $k_1$  mode, as observed. Note also

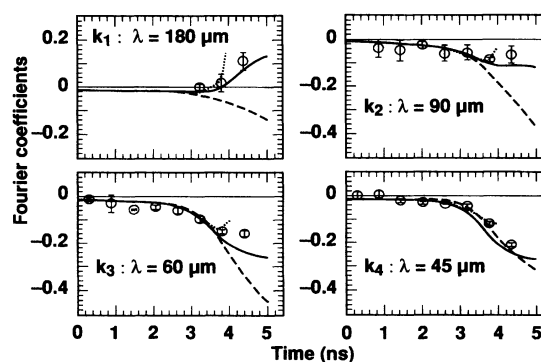


FIG. 5. The open circles represent the experimental Fourier coefficients of  $\ln(\text{exposure})$  vs time for the first four modes of the eight-mode foil. The solid curves represent the corresponding eight-mode simulation with LASNEX, and the dashed curves represent each mode run individually. The dotted curves correspond to a second-order perturbation analysis. All the modeling has been corrected for the instrument spatial resolution.

that the  $k_2$  and  $k_3$  modes saturate for  $t \geq 4$  ns, whereas in the single-mode simulations these modes grow to be quite large. Mode coupling causes a redistribution of the Fourier components, leading to a change in shape of the perturbation, as shown in Fig. 3(b).

The second-order perturbation model described by Eq. (2) is now applied to the eight-mode experiment. The model is formulated in terms of spatial amplitudes, which we define from the LASNEX simulations by

$$\eta(\mu\text{m}) \approx \frac{\delta \int \rho dz}{\rho_{\text{max}}}. \quad (4)$$

Here,  $\rho_{\text{max}}$  and  $\delta \int \rho dz$  represent the foil peak density and modulations in the foil areal density, respectively. For each  $\lambda_n$  in the eight-mode foil, 2D LASNEX simulations are run for very small initial amplitude perturbations, ensuring that the RT evolution remains in the linear regime. The  $\eta_{k_n}^L(t)$  in Eq. (2) are then obtained by scaling by the ratio of actual to the assumed (very small) initial amplitude. This method of generating the  $\eta_{k_n}^L(t)$  from LASNEX automatically includes the effects of the time-dependent acceleration, compression, density gradient, and ablation. The results from the perturbation analysis are shown by the dotted curves in Fig. 5. In the range where the model is applicable,  $t \leq 3.7$  ns, the data are reproduced reasonably well, namely,  $k_2$  and  $k_3$  grow less due to mode coupling and  $k_1$  reverses sign. Beyond  $\sim 3.7$  ns, the effect of coupling on the growth of the dominant modes is no longer insignificant, and the approximations made in the model are no longer valid [15]. We therefore truncate the dotted curves at 4.0 ns.

In conclusion, we have conducted two-mode and eight-mode experiments to examine the effect of multiple modes on perturbation growth. In the linear regime the modes grow independently. In the nonlinear regime, the modes become coupled and the  $k_i \pm k_j$  terms are clearly observed, in agreement with simulations and theory. This coupling leads to a redistribution of the perturbation Fourier composition, corresponding to a change in shape. The bubbles become broader and the spikes narrower. The overall size of the perturbation, however, is not significantly changed.

We wish to acknowledge the assistance of H. Kornblum, D. Phillion, R. Turner, and M. Sacula in drive measurements and foil characterization, useful discussions with M. Dunning, and the highly skilled technical staff at Nova. This work was performed under the auspices of the U.S. DOE by the Lawrence Livermore National Laboratory under Contract No. W-7405-ENG-48.

[1] J.D. Lindl and W.C. Mead, Phys. Rev. Lett. **34**, 1273 (1975).

- [2] S.E. Bodner, Phys. Rev. Lett. **33**, 761 (1974).  
 [3] R.L. McCrory, L. Montierth, R.L. Morse, and C.P. Verdon, Phys. Rev. Lett. **46**, 336 (1981).  
 [4] H. Takabe, K. Mima, L. Montierth, and R.L. Morse, Phys. Fluids **28**, 3676 (1985).  
 [5] M. Tabak, D.H. Munro, and J.D. Lindl, Phys. Fluids B **2**, 1007 (1990).  
 [6] J. Grun, M.E. Emery, C.K. Manka, T.N. Lee, E.A. McLean, A. Mostovych, J. Stamper, S. Bodner, S.P. Obenshain, and B.H. Ripin, Phys. Rev. Lett. **58**, 2672 (1987).  
 [7] J.D. Kilkenny, Phys. Fluids B **2**, 1400 (1990).  
 [8] M. Desselberger, O. Willi, M. Savage, and M. Lamb, Phys. Rev. Lett. **65**, 2997 (1990); Phys. Fluids B **5**, 896 (1993).  
 [9] S.G. Glendinning, S.V. Weber, P. Bell, L.B. DaSilva, S.N. Dixit, M.A. Henesian, D.R. Kania, J.D. Kilkenny, H.T. Powell, R.J. Wallace, P.J. Wegner, J.P. Knauer, and C.P. Verdon, Phys. Rev. Lett. **69**, 1201 (1992).  
 [10] B.A. Remington, S.W. Haan, S.G. Glendinning, J.D. Kilkenny, D.H. Munro, and R.J. Wallace, Phys. Rev. Lett. **67**, 3259 (1991); Phys. Fluids B **4**, 967 (1992).  
 [11] B.A. Remington, S.V. Weber, S.W. Haan, J.D. Kilkenny, S.G. Glendinning, R.J. Wallace, W.H. Goldstein, B.G. Wilson, and J.K. Nash, Phys. Fluids B **5**, 2589 (1993).  
 [12] S.V. Weber, B.A. Remington, S.W. Haan, B.G. Wilson, and J.K. Nash, Report No. UCFL-JC-116225 [Phys. Plasmas (to be published)].  
 [13] S.W. Haan, Phys. Rev. A **39**, 5812 (1989).  
 [14] C.P. Verdon, R.L. McCrory, R.L. Morse, G.R. Baker, D.I. Meiron, and S.A. Orszag, Phys. Fluids **25**, 1653 (1982).  
 [15] S.W. Haan, Phys. Fluids B **3**, 2349 (1991).  
 [16] D. Ofer, D. Shvarts, Z. Zinamon, and S.A. Orszag, Phys. Fluids B **4**, 3549 (1992).  
 [17] R.D. Richtmyer, Commun. Pure Appl. Math. **13**, 297 (1960); E.E. Meshkov, Izv. Akad. Nauk SSSR, Mekh. Zhidk. Gaza **5**, 151 (1969).  
 [18] Guy Dimonte and Bruce Remington, Phys. Rev. Lett. **70**, 1806 (1993).  
 [19] B.A. Hammel, C.J. Keane, T.R. Dittrich, D.R. Kania, J.D. Kilkenny, R.W. Lee, and W.K. Levedahl, J. Quant. Spectrosc. Radiat. Transfer **51**, 113 (1994); Rev. Sci. Instrum. **63**, 5017 (1992).  
 [20] D. Layzer, Astrophys. J. **122**, 1 (1955).  
 [21] E.M. Campbell, Laser Part. Beams **9**, 209 (1991).  
 [22] A. Bar-Shalom, J. Oreg, W.H. Goldstein, D. Shvarts, and A. Zigler, Phys. Rev. A **40**, 3183 (1989).  
 [23] R.J. Ellis, J.E. Trebes, D.W. Phillion, J.D. Kilkenny, S.G. Glendinning, J.D. Wiedwald, and R.A. Levesque, Rev. Sci. Instrum. **61**, 2759 (1990); B.A. Remington, S.G. Glendinning, R.J. Wallace, S. Rothman, and R. Morales, *ibid.* **63**, 5080 (1992); (to be published).  
 [24] H.N. Kornblum, R.L. Kauffman, and J.A. Smith, Rev. Sci. Instrum. **57**, 2179 (1986).  
 [25] G.B. Zimmerman and W.L. Kruer, Comments Plasma Phys. Controlled Fusion **2**, 51 (1975).

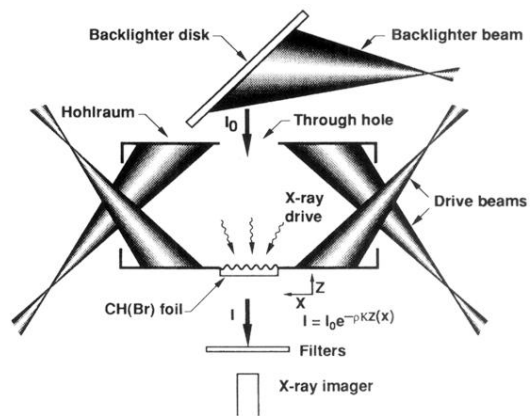


FIG. 1. The experimental configuration consists of a Au cylindrical hohlraum with a modulated CH(Br) foil mounted on the wall. The laser beams convert to x rays in the hohlraum which ablatively accelerate the foil. An additional laser beam generates backlighter x rays used for in flight diagnosis of the foil.